EFFECTS OF CONTROL STRATEGY ON SIZING OF ENERGY STORAGE SYSTEMS FOR PV–WIND POWER PLANTS

Micke Talvi and Kari Lappalainen
Tampere University, Electrical Engineering
E-mail: micke.talvi@tuni.fi, kari.lappalainen@tuni.fi

ABSTRACT: Different control strategies can be used with energy storage systems (ESS) to mitigate power fluctuations of photovoltaic (PV) and wind power plants. Control strategies can significantly affect the required size of the ESS. In this paper, ramp rate (RR), moving average (MA) and low-pass filter (LPF) ESS control strategies are compared for PV, wind, and PV–wind power plants. It was found that the required relative charging and discharging powers of the ESSs were quite similar between the different strategies. For the RR strategy, the required relative ESS energy capacity was found to be the highest and the utilization rate was found to be the lowest among the 3 strategies. The energy level in the ESS was found to behave differently with the RR strategy than with the MA and the LPF strategies. It was also found that with the RR strategy the behavior of the ESS energy level differs between the PV and the wind power plants. With PV power, the energy level of the ESS tends to slowly decline below an initial level during a day, but for wind power, it tends to elevate moderately fast and clearly farther away from the initial level.
Keywords: Photovoltaic power, Wind power, Power fluctuations, Energy storage systems, Control strategy

1 INTRODUCTION

Generated powers of photovoltaic (PV) and wind power plants can fluctuate drastically [1,2], thus the stability of the grid may be endangered. The fluctuating power can be mitigated by energy storage systems (ESS) with different power control strategies. The use of different ESS control strategies has been studied, for instance in [3,4] for PV power plants, but it has not been studied for wind or PV–wind power plants with high resolution output powers of the power plants. A high resolution of power data would be necessary, as the fastest PV power fluctuations may not be detected if the sampling frequency is lower than 1 Hz [5]. In [4], it was found that the applied control strategy significantly affects the size and utilization of the ESSs of PV power plants. In [6], it was found that the relative sizes required for the ESSs are smaller for the wind power (WP) plants than for the PV power plants when a ramp rate (RR) based control strategy was used. Also, the required sizes for the ESSs of the PV–wind power plants were found to be smaller than for the WP plants. Thereby, it would be reasonable to investigate how the applied control strategy affects the sizes of the ESSs of the wind and PV–wind power plants. It would be also useful for ESS planning to find out if there are any differences in the behavior of PV and wind power fluctuations, and how they affect the ESS sizing while using different control strategies.

In this paper, the effects of control strategy on sizing of ESSs for PV–wind power plants are studied. The PV and wind power plants are simulated based on climatic measurements done with a sampling frequency of 10 Hz for a period of 153 days. The applied ESS control strategies are the RR, the moving average (MA) and the low-pass filter (LPF). The goal of this paper is to investigate how the different control strategies affect the requirements and the utilization of the ESSs of PV, wind, and PV–wind power plants.

2 DATA AND METHDOS

2.1 Measurement data

This study is based on the measurements done at the Tampere University Solar PV Power Station Research Plant in Finland [5]. The measured quantities were irradiance, PV module backside temperature, wind speed and ambient temperature. The measurement period was 153 days, starting on 1 June 2019 and ending on 31 October 2019. The sampling frequency for all the measurements was 10 Hz.

The PV power was modeled based on irradiance and PV module backside temperature measurements. Irradiance was measured with a photodiode-based Kipp&Zonen SPLite2 pyranometer. The pyranometer is mounted to a PV module which faces nearly southward and is mounted at a tilt angle of 45°, which is also the tilt angle of the pyranometer. The PV module backside temperature was measured with a National Instruments Pt100 temperature sensor. The WP was modeled based on measured wind speed and ambient temperature. The wind speed was measured with an ultrasonic VAISALA WS425 wind sensor that is mounted at the tip of a pole located at the highest point of the university building. The height from the ground level to the sensor h_1 XXX is 16.13 m. The ambient temperature T_{air} was measured with a VAISALA HMP155 humidity and temperature sensor that is also located on the rooftop of the university building.

The ESS sizing was done for two orders of magnitude: small-scale and large-scale power plants. The nominal powers of the PV and the wind power plants were 10 kW and 3 MW, respectively, for the small- and the large-scale power plants. The nominal powers of the PV–wind power

Table I: Parameter values of the simulation model for the power plants.

Nominal power of the power plant	10 kW	3 MW
Number of PV modules	53	15789
PV module array area	149 m^2	44 340 m^2
Wind turbine height	16.5 m	98 m
Wind turbine swept area	75.4 m^2	5 281 m^2
Calculated power coefficient	0.48	0.50
Wind power time constant	15 s	40 s
Cut-in wind speed	2 m/s	3 m/s
Rated wind speed	9 m/s	16 m/s
Cut-out wind speed	30 m/s	34 m/s

10.4229/EUPVSEC2023/5DV.2.24
020538-001

plants were 20 kW and 6 MW, respectively, for the small- and the large-scale power plants. The PV power plant size was scaled using different numbers of PV modules. The WP plant size was scaled using the quantities of 2 different wind turbine (WT) models [7,8]. Table I presents parameter values used for the power plants.

2.2 PV and wind power modeling

The area of a virtual PV power plant was determined based on the size and tilt angle of the PV modules of the Tampere University Solar PV Power Station Research Plant. The empty space between the PV module rows was determined so that the PV modules would not shade each other during daytime in the summer months in Tampere, Finland. The altitude angle of the Sun was determined to be 20°, and thus the empty space length was determined to be 1916 mm. The length and the width of the PV module were 986 mm and 1475 mm, respectively. The nominal power of the module $P_{\text{nom, PV}}$ was 190 W.

After the suitable empty space length was known, the PV module array areas of the PV power plants were possible to be calculated. As the irradiance was measured only from one sensor, a spatial filter proposed by Marcos et al. [9] was implemented to provide a more realistic irradiance exposure of a PV power plant. The spatial irradiance $G_S(t)$ was calculated as

$$G_S(t) = \frac{G(t)}{\left(\frac{\sqrt{A_{PV}}}{2\pi \cdot 0.0204 \cdot \left(A_{PV}{}^{-0.4997}\right)}\right)s+1}, \quad (1)$$

where $G(t)$ is the measured irradiance, A_{PV} is the PV module array area in hectares and s is the Laplace transform variable. With the spatial filter, the increased smoothing effect of PV power fluctuations could be taken into account, as there are 2 significantly different sizes of PV power plants in this study. The generated PV power P_{PV} was calculated using an equation [10] that takes into account the effect of the PV module temperature T_{PVM} on P_{PV} as

$$P_{PV} = \frac{nP_{\text{nom, PV}}}{G_{STC}} G_S[1 - \beta(T_{PVM} - T_{STC})], \quad (2)$$

where n is the number of the PV modules, G_{STC} is the irradiance in standard test conditions (STC), β is the temperature coefficient and T_{STC} is the temperature in the STC. As the average value for the β was 0.0045 1/°C in [10], this value was used in the calculations of this study as well.

In the WP modeling, the measured wind speed v_1 at the height of h_1 was first extrapolated to the hub heights of the WT models. The extrapolation was done with a power law [11], applied as

$$v_2 = v_1 \left(\frac{h_2}{h_1}\right)^{\alpha}, \quad (3)$$

where v_2 is the extrapolated wind speed at the height of h_2 and α is the shear exponent. Considering the presented values for α in [11], the value for α was determined to be 0.35, as the environment around the wind speed sensor could be considered as a small town but there are a few tall buildings around. Then, the density of the air ρ_{air} was calculated for each data point as [12]

$$\rho_{air} = \frac{p_0}{R_{air}T_{air}} e^{\left(\frac{-gH}{R_{air}T_{air}}\right)}, \quad (4)$$

where p_0 is the standard sea level atmospheric pressure (101325 Pa), R_{air} is the specific gas constant of air (287.05 J/(kg·K)), g is the gravity constant (9.81 m/s^2) and H is the total altitude above sea level. The altitude above sea level for Hervanta Campus of Tampere University, Tampere is 140 m [13], thus the value used for H is the sum of 140 m and the hub height of the WT.

The WP was modeled using the cubic WP equation [12]. First the preliminary WT power $P_{\text{WT, pre}}$ was calculated as

$$P_{\text{WT, pre}}(v_2) = \begin{cases} 0, & v_2 < v_{\text{cut-in}} \\ \frac{1}{2}A_{\text{swept}}\rho_{air}v_2^3 C_p, & v_{\text{cut-in}} \le v_2 < v_{\text{rated}} \\ P_{\text{rated, WT}}, & v_{\text{rated}} \le v_2 < v_{\text{cut-out}} \\ 0, & v_{\text{cut-out}} \le v_2 \end{cases}, \quad (5)$$

where A_{swept} is the swept area of the WT rotor, C_p is the WT power coefficient and $P_{\text{rated, WT}}$ is the rated power of the WT. $v_{\text{cut-in}}$, v_{rated}, and $v_{\text{cut-out}}$ are the cut-in, rated and cut-out wind speeds of the WT, respectively. The values of C_p needed to be calculated for the WTs using Eq. (5), as they were not available. The calculated maximum values were used as the C_p values for the WTs, as that would provide sufficient accuracy according to [14]. The $v_{\text{cut-in}}$, v_{rated}, and $v_{\text{cut-out}}$ values as well as the calculated C_p values of the WTs are presented in Table I.

A low-pass filter was applied to take the inertia of the WT rotor [15] into account and to level the power fluctuations of $P_{\text{WT, pre}}$ to a more realistic level. The smoothed wind power P_{wind} was acquired by applying the first-order low-pass filter to $P_{\text{WT, pre}}$ as

$$P_{\text{wind}}(t) = \frac{P_{\text{WT, pre}}(t)}{\tau_{WT}s+1}, \quad (6)$$

where τ_{WT} is the time constant of the WT. The τ_{WT} values for the WTs are presented in Table I. With these τ_{WT} values, P_{wind} should not be oversmoothed. The PV and wind power models were presented in more detail in [6].

2.3 Control strategies

The applied control strategies of this study are presented here shortly. With the combined PV–wind power plants, P_{PV} and P_{wind} were first summed, then the sum power was treated by the control strategy. The goal of the control strategies was to keep the power fluctuations of a power plant under the RR limit of 10 %/min. For the MA and the LPF strategies, the time constants were also iterated to be as small as possible. If the time constants were too large, the results would not be that comparable between the different strategies, as the MA and the LPF strategies would smooth the output power significantly more than the RR strategy. The amount of energy stored in the ESS was selected to be the same in the beginning of each day, i.e., the ESS was assumed to be charged or discharged back to the same initial energy level at midnight.

The RR control strategy limits the change in the power fed to the grid P_{grid} between two consecutive time stamps. The RR control strategy first checks the maximum upward power ramp as

$$P_{\text{grid, 1}}(i) = \min\left(P_{PP}(i), \left(P_{\text{grid, RR}}(i-1) + RR10PP\right)\right), \quad (7)$$

10.4229/EUPVSEC2023/5DV.2.24
020538-002

where $P_{\text{grid, 1}}(i)$ is the preliminary power fed to the grid that does not exceed the maximum power RR of the power plant *RR10PP* that is determined by the RR limit of 10 %/min, $P_{\text{grid, RR}}(i\text{-}1)$ is the power fed to the grid at the time step i-1 and $P_{\text{PP}}(i)$ is the power of the power plant at the time step i. Then, the RR control strategy checks the maximum downward power ramp as

$$P_{\text{grid, RR}}(i) = \max\left(P_{\text{grid, 1}}(i), \left(P_{\text{grid, RR}}(i-1) - RR10PP\right)\right). \quad (8)$$

Now, $P_{\text{grid, RR}}(i)$ does not exceed the RR limit of 10 %/min during either the upward or the downward power ramp. The power of the ESS P_{ESS} is then determined as

$$P_{\text{ESS}}(i) = P_{\text{PP}}(i) - P_{\text{grid, RR}}(i). \quad (9)$$

In the MA control strategy, the power fed to the grid $P_{\text{grid, MA}}(i)$ is determined as a moving average as

$$P_{\text{grid, MA}}(i) = \frac{\sum_{j=i-\tau_{\text{MA}}+1}^{i} P_{\text{PP}}(j)}{\tau_{\text{MA}}}, \quad (10)$$

where τ_{MA} is the MA control strategy time constant of the power plant. After $P_{\text{grid, MA}}(i)$ is determined, $P_{\text{ESS}}(i)$ is determined according to Eq. (9).

In the LPF control strategy, the P_{PP} is first filtered using first-order low-pass filter as

$$P_{\text{grid, LPF}}(t) = \frac{P_{\text{PP}}(t)}{\tau_{\text{LPF}}s+1}, \quad (11)$$

where $P_{\text{grid, LPF}}(t)$ is the power fed to the grid with the LPF control strategy and τ_{LPF} is the LPF control strategy time constant of the power plant. After that, P_{ESS} is determined according to Eq. (9).

3 RESULTS AND DISCUSSION

3.1 Small-scale power plants

The ESS sizing results for the small-scale power plants are presented in this subchapter. The results are explained by an example day of June 22, 2019. The simulated 10 kW PV power and the powers fed to the grid for the RR, the MA and the LPF strategies are presented in Fig. 1 (a). The energy levels stored in the ESS of the 10 kW PV power plant with the control strategies are presented in Fig. 1 (b). It can be seen clearly that the MA and the LPF strategies smooth the original P_{PV} a lot more than the RR strategy. Although, all the graphs of the control strategies fluctuate significantly slower than the original P_{PV}.

The different behaviors of the control strategies can be seen also in Fig. 1 (b). The graphs of the MA and the LPF strategies stay above 0 kWh the whole example period and are very similar, whereas the graph of the RR strategy stays below 0 kWh from around 09:00 onwards, and its highest peak has significantly higher amplitude than with the MA and the LPF strategies. The small peaks of the MA and the LPF graphs at around 05:50 in Fig. 1 (b) were caused by a moderately high upward ramp of the P_{PV}. However, the highest RR of this fluctuation did not exceed the RR limit, and thus, the RR strategy did not smooth it.

Table II presents the ESS sizing results for the 10 kW PV power plant. The highest observed RRs of the different

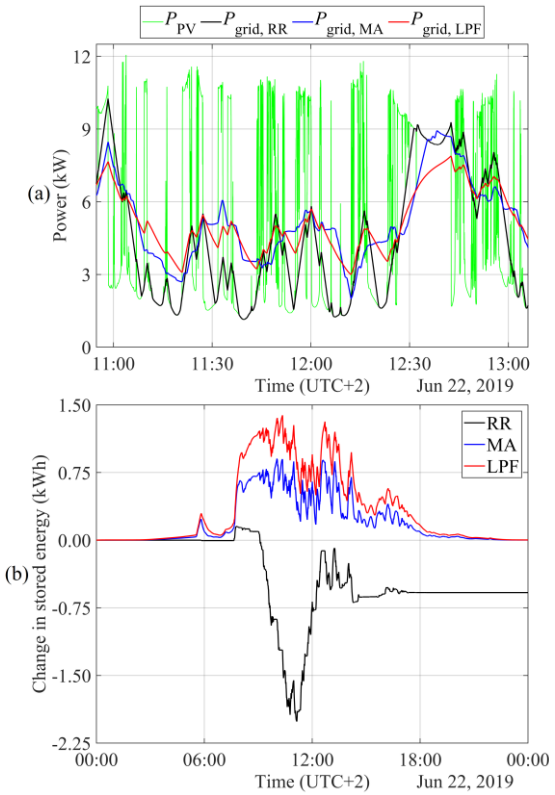

Figure 1: Example of simulated 10 kW PV power, powers fed to the grid for the RR, MA, and LPF strategies (a) and change of the ESS energy level from the initial energy level with the RR, MA, and LPF strategies (b).

strategies are quite close each other. The relative energy capacity requirements for the ESS seem to differ significantly between the strategies, with the MA strategy having the lowest requirement and the RR strategy having the highest. The relative charging and discharging power values seem to be very similar between the strategies, however. The MA and the LPF strategies seem to utilize the ESS significantly more than the RR strategy, as their daily maximum shares of energy cycled through the ESS are roughly 66% higher than the share for the RR strategy. The high utilization rate of the ESS with the MA and the LPF control strategies was found also in [4]. In [4], it was stated that using the RR control strategy for the ESS of the PV power plant would result in a smaller-sized ESS than

Table II: Iterated time constants, the highest observed power ramp rates and the ESS sizing results with the control strategies for the 10 kW PV power plant.

Control strategy	RR	MA	LPF
Time constant (s)	-	725	60.0
Highest observed RR (%/min)	10.0	9.67	9.53
Relative energy capacity (h)	0.245	0.0964	0.149
Relative charging power capacity (%)	0.877	0.944	0.947
Relative discharging power capacity (%)	0.779	0.770	0.730
Daily maximum share of energy cycled through the ESS (%)	0.130	0.214	0.218

10.4229/EUPVSEC2023/5DV.2.24
020538-003

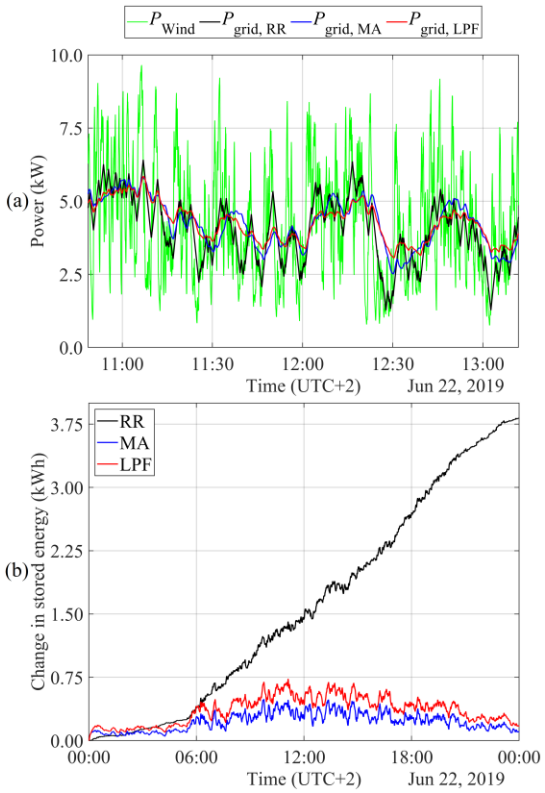

Figure 2: Example of simulated 10 kW wind power, powers fed to the grid for the RR, MA, and LPF strategies (a) and change of the ESS energy level from the initial energy level with the RR, MA, and LPF strategies (b).

use of the MA and the LPF strategies. However, in this study, the values for the relative energy capacity of the ESS of the 10 kW PV power plant with the MA and the LPF strategies are significantly smaller than the value with the RR strategy. The reason for this is explained in Section 3.3.

Fig. 2 (a) presents the simulated 10 kW WP and the powers fed to the grid for the RR, the MA and the LPF strategies. The powers fed to the grid seem to behave in a similar way as with the 10 kW PV power plant – the graphs of the MA and the LPF strategies staying smoother than the graph of the RR strategy. The energy levels stored in the ESS of the 10 kW WP plant with the control strategies are presented in Fig. 2 (b). It can be seen that the graphs of the MA and the LPF strategies behave very similarly, but the graph of the RR strategy behaves

Table III: Iterated time constants, the highest observed power ramp rates and the ESS sizing results with the control strategies for the 10 kW wind power plant.

Control strategy	RR	MA	LPF
Time constant (s)	-	565	45.0
Highest observed RR (%/min)	10.0	9.43	9.56
Relative energy capacity (h)	0.576	0.0601	0.0875
Relative charging power capacity (%)	0.668	0.735	0.717
Relative discharging power capacity (%)	0.527	0.529	0.478
Daily maximum share of energy cycled through the ESS (%)	0.129	0.216	0.208

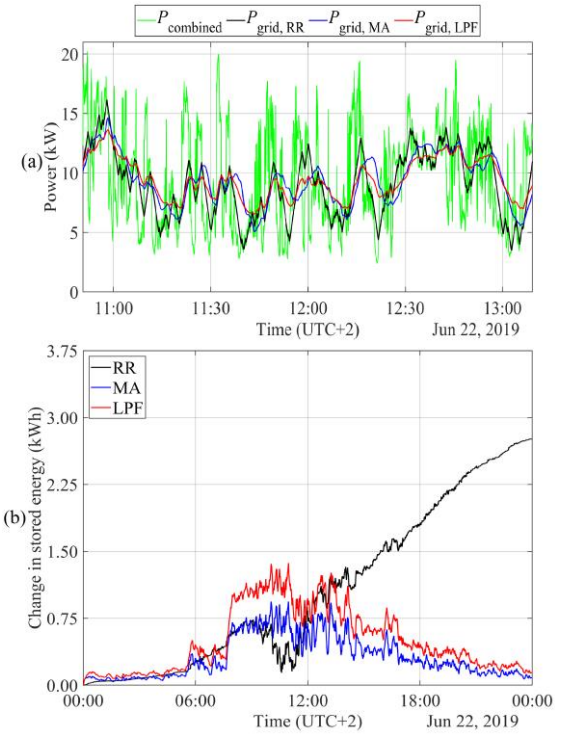

Figure 3: Example of simulated combined 20 kW PV–wind power, powers fed to the grid for the RR, MA, and LPF strategies (a) and change of the ESS energy level from the initial energy level with the RR, MA, and LPF strategies (b).

significantly differently and its highest value is roughly 8 and 5 times the highest values of the graphs of the MA and the LPF strategies, respectively.

Table III presents the ESS sizing results for the 10 kW WP plant. The highest observed RRs of the different strategies are quite similar. The relative energy capacity of the ESS required with the RR strategy differs significantly from the values of the MA and the LPF strategies. This can be seen also in Fig. 2 (b). The relative power capacity values of the ESS are quite similar between the different strategies for the 10 kW WP plant. The daily maximum share of energy cycled through the ESS with the RR strategy is clearly smaller than with the MA and the LPF strategies.

When comparing the results of the 10 kW PV and the 10 kW wind power plant, on general, the ESS sizing values are higher for the 10 kW PV power plant than for

Table IV: Iterated time constants, the highest observed power ramp rates and the ESS sizing results with the control strategies for the 20 kW PV–wind power plant.

Control strategy	RR	MA	LPF
Time constant (s)	-	483	36.0
Highest observed RR (%/min)	10.0	9.94	9.45
Relative energy capacity (h)	0.233	0.0489	0.0715
Relative charging power capacity (%)	0.587	0.590	0.565
Relative discharging power capacity (%)	0.135	0.154	0.141
Daily maximum share of energy cycled through the ESS (%)	0.100	0.190	0.183

10.4229/EUPVSEC2023/5DV.2.24
020538-004

the 10 kW WP plant, in line with the results of [6]. In Tables II and III, the only notable exception is that the value of the relative energy capacity of the ESS required with the RR strategy for the 10 kW WP plant is roughly 2.4 times the value for the 10 kW PV power plant. This difference can be seen also from Figs. 1 (b) and 2 (b). The reason for the difference is explained in Section 3.3.

Fig. 3 (a) presents the simulated 20 kW PV–wind power and the powers fed to the grid for the RR, the MA and the LPF strategies. The powers fed to the grid seem to behave again in a similar way as with the separate 10 kW PV and wind power plants. Fig. 3 (b) presents the energy levels stored in the ESS with the control strategies. It can be seen that the graphs of the MA and the LPF strategies resemble the corresponding graphs of Figs. 1 (b) and 2 (b). In Fig. 3 (b), the graph of the RR strategy seems to resemble the combination of the corresponding graphs of Figs. 1 (b) and 2 (b). However, the graph of the RR strategy never goes below 0 kWh for the 20 kW PV–wind power plant.

Table IV presents the ESS sizing results for the 20 kW PV–wind power plant. The relative energy capacity of the ESS with the RR strategy again differs from the values of the MA and the LPF strategies. Apart from the relative energy capacity of the ESS with the RR strategy, the ESS sizing values are clearly smaller for the 20 kW PV–wind power plant than for the 10 kW PV and wind power plants. In [6], it was found also that the required relative ESS size for the combined PV–wind power plant is smaller than for the PV power plant considering the small-scale power plants. However, the difference between the ESSs of the small-scale wind and PV–wind power plants, was minimal in [6].

3.2 Large-scale power plants

The ESS sizing results for the large-scale power plants are presented in this subchapter. Only the energy levels stored in the ESS are presented in this subchapter as figures, as the graphs of the simulated powers of the large-scale power plants were very similar to the corresponding graphs of the small-scale power plants in Section 3.1. Evolutions of the energy amounts stored in the ESSs of the 3 MW PV, the 3 MW wind, and the 6 MW PV–wind power plants with the control strategies are presented in Figs. 4 (a), 4 (b) and 4 (c), respectively. The graphs of Fig. 4 (a) are very similar to the graphs of Fig. 1 (b).

The graphs of the MA and the LPF strategies for the 3 MW WP plant in Fig. 4 (b) resemble the corresponding graphs of the 10 kW WP plant in Fig. 2 (b). The graph of the RR strategy for the 3 MW WP plant does not ascend as fast or as high as for the 10 kW WP plant in Fig. 2 (b). The graph of the RR control strategy for the 6 MW PV–wind power plant in Fig. 4 (c) is quite different than the corresponding graph of Fig. 3 (b), as the graph of the RR control strategy for the 6 MW PV–wind power plant stays negative for a couple hours during the example period.

Table V presents the ESS sizing results for the 3 MW PV power plant. The relative ESS sizing requirements are slightly lower for the 3 MW PV power plant than for the 10 kW PV power plant. This is expected, as the increased spatial smoothing of the larger PV power plant decreases the PV power fluctuations relatively, as found in [1].

Table VI presents the ESS sizing results for the 3 MW WP plant. When comparing these results to the results of the 10 kW WP plant in Table III, the required relative power capacity and the utilization rate of the ESS are smaller for the 3 MW WP plant. The required relative energy capacity value of the ESS is also smaller for the 3 MW WP plant than for the 10 kW WP plant when using the RR control strategy, but with the MA and the LPF strategies, the relative energy requirements for the 3 MW WP plant are slightly larger than for the 10 kW WP plant.

Table VII presents the ESS sizing results for the 6 MW

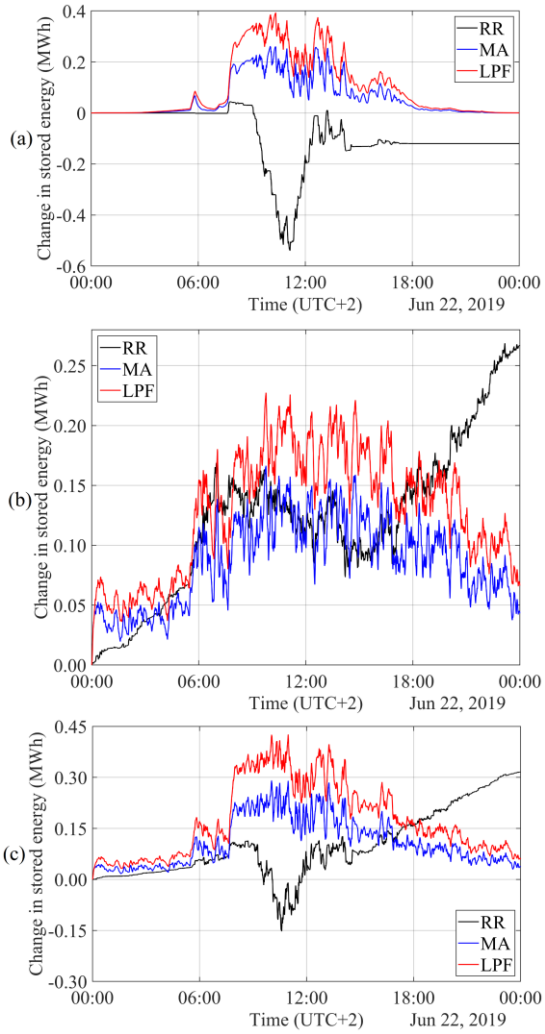

Figure 4: Example of change in the energy stored in the ESS from the initial energy level during a day for the 3 MW PV (a), the 3 MW wind (b), and the 6 MW PV–wind (c) power plants with the RR, MA, and LPF strategies.

Table V: Iterated time constants, the highest observed power ramp rates and the ESS sizing results with the control strategies for the 3 MW PV power plant.

Control strategy	RR	MA	LPF
Time constant (s)	-	705	57.0
Highest observed RR (%/min)	10.0	9.63	9.57
Relative energy capacity (h)	0.215	0.0938	0.142
Relative charging power capacity (%)	0.821	0.909	0.909
Relative discharging power capacity (%)	0.757	0.761	0.717
Daily maximum share of energy cycled through the ESS (%)	0.123	0.208	0.212

10.4229/EUPVSEC2023/5DV.2.24
020538-005

Table VI: Iterated time constants, the highest observed power ramp rates and the ESS sizing results with the control strategies for the 3 MW wind power plant.

Control strategy	RR	MA	LPF
Time constant (s)	-	515	38.0
Highest observed RR (%/min)	10.0	9.64	9.54
Relative energy capacity (h)	0.302	0.0642	0.0882
Relative charging power capacity (%)	0.501	0.627	0.604
Relative discharging power capacity (%)	0.453	0.487	0.427
Daily maximum share of energy cycled through the ESS (%)	0.0734	0.161	0.145

Table VII: Iterated time constants, the highest observed power ramp rates and the ESS sizing results with the control strategies for the 6 MW PV–wind power plant.

Control strategy	RR	MA	LPF
Time constant (s)	-	430	34.0
Highest observed RR (%/min)	10.0	9.81	9.32
Relative energy capacity (h)	0.114	0.0506	0.0751
Relative charging power capacity (%)	0.518	0.531	0.528
Relative discharging power capacity (%)	0.100	0.142	0.141
Daily maximum share of energy cycled through the ESS (%)	0.0536	0.139	0.130

PV–wind power plant. The required relative energy capacity values of the ESS with the MA and the LPF strategies are slightly higher for the 6 MW PV–wind power plant than for the 20 kW PV–wind power plant in Table IV. However, the other ESS sizing values between these power plants are smaller for the 6 MW PV–wind power plant.

In conclusion, the relative power requirements and utilization rates of the ESS were lower for the large-scale power plants than for the small-scale ones with all 3 control strategies. The relative ESS energy requirement was also lower the large-scale power plants except for WP and the combined PV–wind power when the MA or LPF strategy was used.

3.3 Typical ESS cycles with PV and wind power

This subchapter shortly analyses the differences between the typical ESS cycles with PV and wind power. The typical ESS cycles with PV and wind power are the main reason behind the significantly different graphs of the evolution of the energy amounts stored in the ESS controlled by the RR strategy between PV and wind power plants seen in Figs. 1 (b) and 2 (b), for instance. Fig. 5 (a) presents the typical ESS cycles with PV power and Fig. 5 (b) presents the typical ESS cycles with WP. The typical ESS cycles are illustrated as red and blue boxes, respectively, for the PV and the wind power.

In Fig. 5 (a), the P_{PV} typically fluctuates from one power level to another (one ESS charging or discharging cycle) so that it exceeds the RR limit in the same direction with multiple narrow peaks or fewer wide peaks. After the transition, the P_{PV} stays at a certain level, corresponding to unshaded or shaded PV power plant, for a period, and only

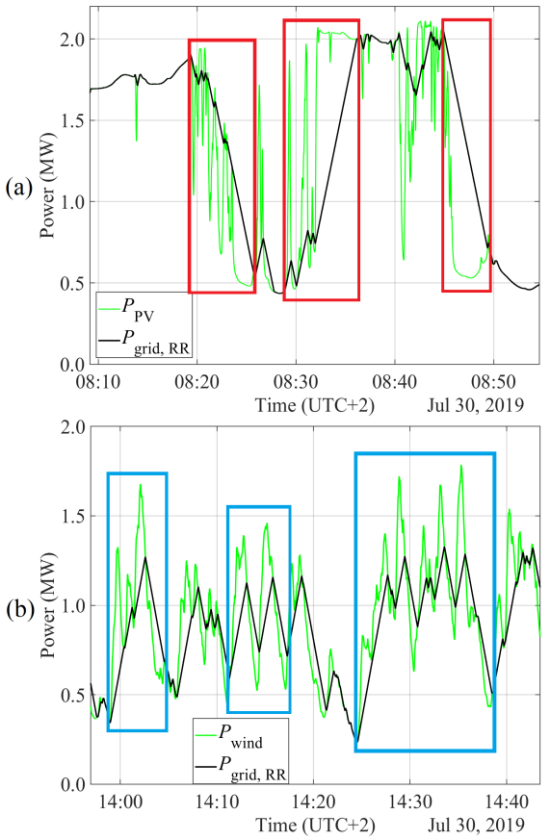

Figure 5: Example of typical ESS cycles with PV (a) and wind (b) power.

after then it seems to fluctuate to the other level. As the P_{PV} remains quite steady after the short fluctuations, the gradually moving $P_{grid, RR}$ can also reach the same level as the P_{PV}. Due to this behavior, the ESS typically only either charges or discharges power during one typical ESS cycle with PV power. In the long run, the energy level of the ESS will start to slowly decline below 0, as seen in Figs. 2 (b) and 5 (b). One reason for this is that typically the front edges of cloud shadows are sharper than the back edges [16]. Thus, the P_{PV} typically drops faster when a cloud shadow covers the PV power plant than it comes back up after the cloud has passed. This means that, during the arrival of the cloud the P_{PV} deviates more from the $P_{grid, RR}$ than during the departure of the cloud. This causes that the ESS is discharged more than charged, and thus, its energy level keeps declining in the long run.

In Fig. 5 (b), the P_{wind} fluctuates so that during one typical ESS cycle the P_{wind} first fluctuates upward, and then instantly it fluctuates downward. The P_{wind} usually exceeds the $P_{grid, RR}$ in both directions during the typical ESS cycle. However, as the downward fluctuation follows the upward fluctuation instantly, the $P_{grid, RR}$ does not reach the level of the upward fluctuation peak of the P_{wind}. Thus, the final upward peak of the P_{wind} always remains higher than the $P_{grid, RR}$. This results in that there is more power to be charged than discharged during one typical ESS cycle with WP, and thus, the energy level in the ESS of a WP plant keeps gradually ascending through the day, as seen in Figs. 2 (b) and 4 (b).

This phenomenon can be explained also by a more visual point-of-view. When observing the red boxes of Fig. 5 (a), it can be seen that the P_{PV} remains roughly only either above or below the $P_{grid, RR}$ during one typical ESS

10.4229/EUPVSEC2023/5DV.2.24
020538-006

cycle with PV power. The areas between the P_{PV} and the $P_{grid,RR}$ are roughly similar when comparing a typical ESS cycle with either an upward or a downward ramp of the $P_{grid,RR}$. As these areas are similar in size, this results in that the net flow of energy through the ESS of a PV power plant is nearly 0. However, the energy level declines gradually due to the aforementioned differences between upward and downward PV power fluctuations.

When observing the blue boxes of Fig. 5 (b), it can be seen that the P_{wind} fluctuates both above and below the $P_{grid,RR}$ inside one blue box. This means that the ESS of a WP plant charges and discharges power during one typical ESS cycle. However, as the area between the P_{wind} and the $P_{grid,RR}$ is clearly larger during the upward part of the $P_{grid,RR}$ ramp, the ESS of a WP plant will be charged more than discharged during a typical ESS cycle with WP. This will result in the constantly elevating energy level stored in the ESS during the day. Thus, the relative energy requirement for an ESS controlled by the RR strategy is higher for WP plants than for PV power plants.

The reason why this phenomenon emerges only with the RR strategy, is that the data steps are not tied to each other with the RR strategy on contrary to the MA and the LPF strategies. As the current data step is not tied to older steps, the energy level of an ESS of a PV or a wind power plant can progress considerably far away from 0. The phenomenon is stronger for the small-scale power plants than for the large-scale ones as the WP fluctuations smoothen with increasing turbine size. In this study, the amount of energy stored in the ESS was selected to be the same in the beginning of each day. Thus, the effect of this phenomenon in the long term was not studied but only daily ESS requirements were considered.

4 CONCLUSIONS

This paper presented a study of the effects of the control strategy on sizing of ESSs for small- and large-scale PV, wind, and PV–wind power plants. The output powers of the power plants were modeled based on climatic measurements. The power plants and the ESSs of this study were virtual. The chosen ESS control strategies were the RR, the MA and the LPF strategies.

It was found that the MA and the LPF control strategies resulted in very similar behaviors and sizes of the ESSs. The RR control strategy seemed to differ significantly from the 2 other strategies with its ESS usage behavior and ESS sizing results considering the required relative energy capacity and the utilization rate of the ESS. The relative power requirements and utilization rates of the ESS were lower for the large-scale power plants than for the small-scale ones with all studied control strategies. The relative ES energy requirement was lower for the large-scale power plants except for the WP plants and the combined PV–wind power plants when the ESS was controlled by the MA or LPF strategy.

Differences were also found in the ESS usage behaviors and the ESS sizing results between the PV and the wind power plants. The reason for the different behaviors of the ESS energy levels of the PV and the wind power plants, was that the typical ESS cycles are different for PV and wind power. Based on the results of this paper, control strategies can significantly affect the required size and the usage behavior of the ESS for PV, wind, and PV–wind power plants.

ACKNOWLEDGMENTS

We acknowledge the financial support from Business Finland for the research reported in this paper. K. Lappalainen was funded by the Research Council of Finland (funding decision 348701).

REFERENCES

[1] J. Marcos, L. Marroyo, E. Lorenzo, D. Alvira, E. Izco, Progress in Photovoltaic Research and Applications 19 (2011) 218. https://doi.org/10.1002/pip.1016.
[2] B.K. Parsons, Y. Wan, B. Kirby, Proceedings of the European Wind Energy Conference (2001).
[3] J. Martins, S. Spataru, D. Sera, D.-I. Stroe, A. Lashab, Energies 12 (2019) 1342. https://doi.org/10.3390/en12071342.
[4] S. Sukumar, M. Marsadek, K.R. Agileswari, H. Mokhlis, Journal of Energy Storage 20 (2018) 218. https://doi.org/10.1016/j.est.2018.09.013.
[5] D. Torres Lobera, A. Mäki, J. Huusari, K. Lappalainen, T. Suntio, S. Valkealahti, International Journal of Photoenergy 2013 (2013) 837310. https://doi.org/10.1155/2013/837310.
[6] M. Talvi, T. Roinila, K. Lappalainen, Energies 16 (2023) 4313. https://doi.org/10.3390/en16114313.
[7] RyseEnergy. Available online (accessed on 8.9.2023): https://www.ryse.energy/10kw-wind-turbines/.
[8] Wind-Watch. Available online (accessed on 8.9.2023): https://docs.wind-watch.org/Enercon.pdf.
[9] J. Marcos, L. Marroyo, E. Lorenzo, D. Alvira, E. Izco, Progress in Photovoltaics: Research and Applications 19 (2011) 505. https://doi.org/10.1002/pip.1063.
[10] E. Skoplaki, J.A. Palyvos, Solar Energy 83 (2009) 614. https://doi.org/10.1016/j.solener.2008.10.008.
[11] F.A. Hadi, International Journal of Advanced Research in Electrical, Electronics and Instrumentation Engineering 4 (2015) 8176. DOI: 10.15662/IJAREEIE.2015.0410058.
[12] L. Söder, T. Ackermann, Wind Power in Power Systems 1st ed. (2005) 25.
[13] Maanmittauslaitos—Karttapaikka. Available online (accessed on 8.9.2023): https://asiointi.maanmittauslaitos.fi/karttapaikka/.
[14] C. Carrillo, A.F. Obando Montaño, J. Cidrás, E. Díaz-Dorado, Renewable and Sustainable Energy Reviews 21 (2013) 572. https://doi.org/10.1016/j.rser.2013.01.012.
[15] C. Tang, M. Pathmanathan, W.L. Soong, N. Ertugrul, Proceedings of the 2008 Australasian Universities Power Engineering Conference (2008).
[16] K. Lappalainen, S. Valkealahti, Solar Energy 112 (2015) 55. https://doi.org/10.1016/j.solener.2014.11.018.